Fabrication of Fischer–Tropsch Catalysts by Deposition of Iron Nanocrystals on Carbon Nanotubes

Marianna Casavola, Justus Hermannsdörfer, Niels de Jonge, A. Iulian Dugulan, and Krijn P. de Jong**

The fabrication of supported catalysts consisting of colloidal iron oxide nanocrystals with tunable size, geometry, and loading—homogeneously dispersed on carbon nanotube (CNT) supports—is described herein. The catalyst synthesis is performed in a two-step approach. First, colloidal iron and iron oxide nanocrystals with a narrow size distribution are produced. Second, the nanocrystals are attached to CNT grains serving as support structure. Important features, like iron loading and nanocrystal density on the CNT support, are controlled by changing the nanocrystal concentration and ligand concentration, respectively. The Fischer–Tropsch performance reveals these new materials to be active, selective toward lower olefins (60% C of hydrocarbons produced in the absence of promoters), and remarkably stable against particle growth.

1. Introduction

Supported metal nanocrystals catalyze a realm of industrially relevant reactions for the selective production of chemicals and transportation fuels. Relevant to their wide application in heterogeneous catalysis, improvements in catalyst performance and understanding of key features often critically depend on progress in catalyst synthesis. Conventional methods, such as incipient wetness impregnation and deposition precipitation, allow a limited structural control and often give rise to a broad distribution of nanoparticle size and limited control over interparticle spacing on the support. This represents a considerable limitation, since fundamental catalytic features, such as activity, product selectivity, and stability, depend on several structural parameters. It is therefore very important to fabricate catalysts with controllable characteristics as model systems to shed light on the relationships between catalyst structure and performance.[1–3]

The Fischer–Tropsch (FT) synthesis is a key process for the synthesis of fuels and chemicals from alternative feedstock and a major example of a structure-sensitive process.[4–7] Supported iron-based catalysts have shown promising results for conversion of synthesis gas (a mixture of H_2 and CO) to olefins, a process also referred to as Fischer Tropsch to Olefins (FTO). Compared to catalysts based on cobalt and other metals, iron has several advantages, in particular, it can disfavor secondary hydrogenation reactions, thus producing olefins with high selectivity. Catalyst stability being one of the major issues, supported catalysts give better results than their bulk counterparts. Supported iron catalysts have shown excellent catalytic performance and improved stability over time due to the higher dispersion and catalytic surface available.[8,9] Nevertheless, the relationships of activity, selectivity, promoter effects, and nanoparticle size are still object of debate.[6,8] Catalyst nanocrystals undergo severe phase changes during activation and syngas exposure and nanocrystals of different size and faceting can present unequal degrees of surface reduction and carburization, thus giving an unequal contribution to the overall catalyst performance.[10–12] In order to improve the knowledge of these relevant features, it would be essential to fabricate catalysts with well-controlled nanocrystal size, composition, and spacing on the support material.

Nanoscience has provided in principle the tools to fabricate catalysts with precisely tunable characteristics that, however, have been exploited for actual heterogeneous catalytic applications to a limited extent only. Among different synthesis methods, the colloidal route provides superior results in terms of quality and versatility of the fabricated nanocrystals. This wet-chemical synthetic approach allows unprecedented control over size, shape, and crystallinity of the nanocrystals, which can be successively processed and transferred to dedicated substrates according to the application. Despite limitations, mainly concerning the scaling up of the synthesis procedures, the use of colloidal nanocrystals in heterogeneous catalysis is extremely promising for fundamental studies[13–15] and even one industrial application has already been reported.[16] Merging of catalysis and nanomaterial chemistry routes could pave the

Dr. M. Casavola, Prof. K. P. de Jong
Inorganic Chemistry and Catalysis
Debye Institute for Nanomaterials Science
Utrecht University
Universiteitsweg 99, 3584 CG, Utrecht, The Netherlands
E-mail: m.casavola@uu.nl; K.P.deJong@uu.nl
Dr. J. Hermannsdörfer, Prof. N. de Jonge
INM–Leibniz Institute for New Materials
Campus D2 2, 66123 Saarbrücken, Germany
Dr. A. I. Dugulan
Fundamental Aspects of Materials and Energy Group
Delft University of Technology
Mekelweg 15, 2629 JB, Delft, The Netherlands

DOI: 10.1002/adfm.201501882

way to the design of catalysts consisting of metal nanocrystals of the same size and composition, equally spaced on a desired substrate.

The literature offers a few examples of the use of colloidal nanocrystals for heterogeneous catalysis and in particular to improve the nanocrystal dispersion in FT catalysts.[6,13–27] In these contributions, the deposition of the nanocrystals on the substrate is performed by deposition precipitation or impregnation of the substrate with a suspension of nanocrystals in the liquid phase, or by destabilizing the colloidal suspension by the addition of a nonsolvent,[13,17] which can eventually cause aggregation of the nanocrystals. In these methods, it is crucial to functionalize the support in order to improve the wettability of the substrate surface with the organic suspension[13,17] or to generate anchoring points on the support surface for the nanocrystal attachment.[6,17] The regulation of the nanocrystal-support interaction is fundamental, since on the one hand a weak binding can cause nanocrystal aggregation during calcination and/or catalytic tests, while on the other hand a strong binding could cause a retarded reducibility and limited reactivity of the nanocrystals. These parameters play a relevant role in iron-based FT catalysts too, and it has been demonstrated in previous work that iron nanoparticles anchored on weakly interactive supports, like alpha-alumina and carbon nanofibers, show excellent FTO performance.[8] Compared to oxidic supports, carbon supports have been advantageously used in FT catalysis, since they weakly interact with metal catalysts and could improve their reducibility.[28–35] Carbon nanotubes (CNTs) used in this study are chemically and thermally stable and due to their high surface to volume ratio and large mesopore volume can sustain high metal loadings.

In the present work, we study the formation of CNT-supported iron-based catalysts, consisting of colloidal iron/iron oxide nanocrystals with controlled size and composition, uniformly attached to nonfunctionalized, weakly interacting CNT supports. These catalysts have been fabricated via wet-chemical methods in a two-step approach, based on the synthesis of colloidal iron and iron oxide nanocrystals and their successive anchoring to CNT supports. We observed that temperature and ligand concentration play a key role in controlling the diffusion of the metal nanoparticles within the skein of macroscopic CNT grains (sieve fraction 200–400 μm) and their uniform attachment on the CNTs. We verified that ligands can be finally removed upon drying, and the catalysts were active for the FT conversion of synthesis gas with high selectivity to C_2–C_4 olefins.

2. Results and Discussion

Nanocrystals in the 3–14 nm range were synthesized according to the procedure published by Buonsanti et al.[36,37] By changing experimental parameters, like temperature and the amount of precursor injected, it was possible to achieve a high control over the nanocrystal size in the 3–14 nm range with a narrow size dispersion (polydispersity 5%–10%) as shown in the overview in **Figure 1**a–f. For comparison, we also synthesized iron nanocrystals in the 10–20 nm range (Figure 1g) and iron oxide nanocrystals in the 50–100 nm range (Figure 1h) by following two different protocols.[38,39]

In a successive step, the iron oxide nanocrystals were assembled on CNT support particles by heating a mixture of the two

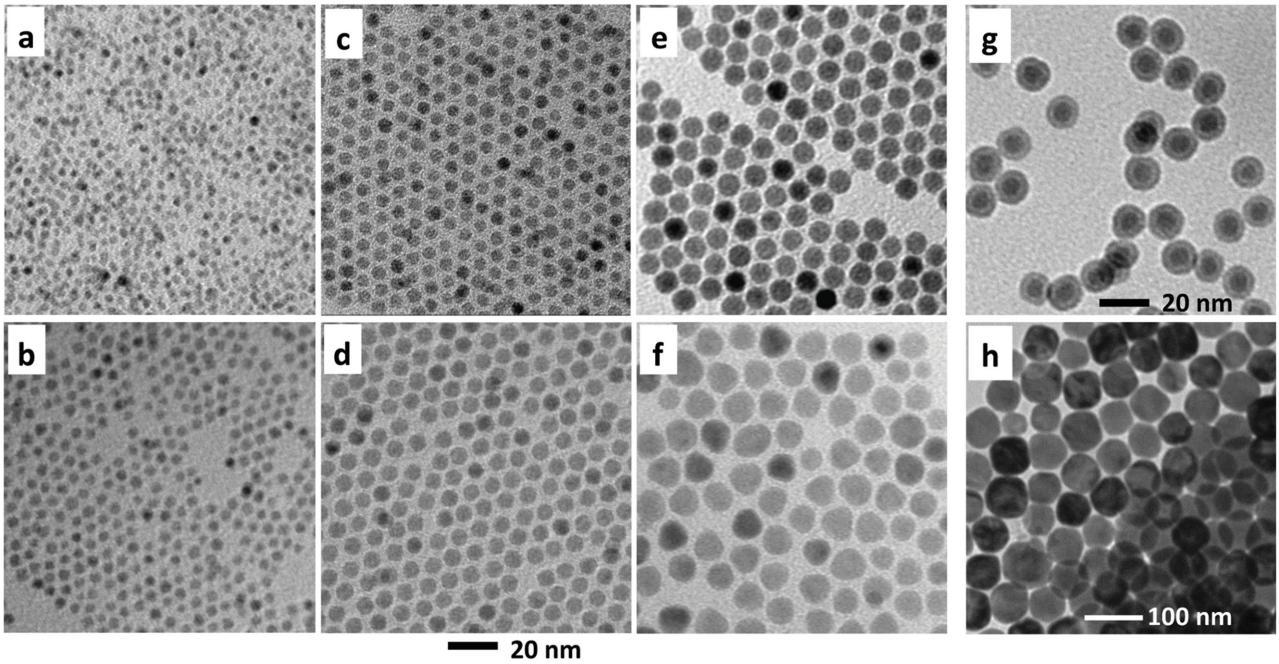

Figure 1. Transmission electron microscopy (TEM) images of iron-based colloidal nanocrystals with different size. Iron oxide colloidal nanocrystals of a) 3 ± 0.4, b) 4 ± 0.4, c) 5.5 ± 0.4, d) 8 ± 0.6, e) 10 ± 0.8, and f) 14 ± 1 nm diameter; the scale bar is 20 nm. g) Iron–iron oxide core–shell nanocrystals of 14.7 ± 0.8 nm diameter; h) iron oxide nanocrystals of 67 ± 8 nm diameter. The nanocrystal average size has been determined by a statistics on around 300 nanocrystals based on TEM images.

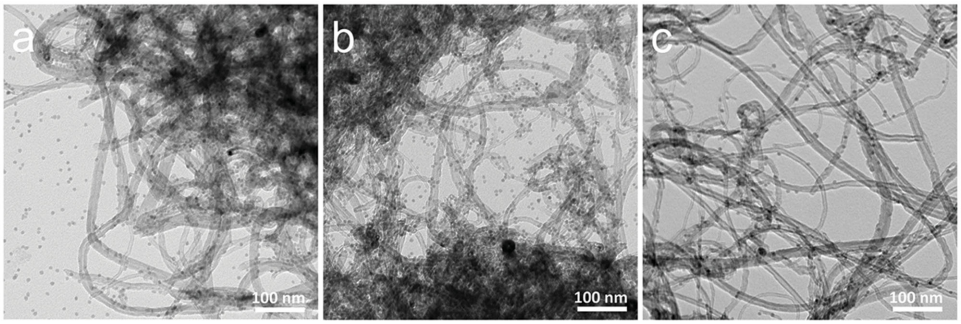

Figure 2. TEM overview of CNT–iron oxide nanocrystal (7 nm diameter) samples withdrawn from the reaction mixture at different stages, i.e., a) after 7 min stirring, when the mixture has reached a temperature of 130 °C; b) after stirring at a constant temperature of 200 °C for 2 min; c) after stirring at a constant temperature of 200 °C for 30 min.

in octadecene solvent. In a typical experiment, a stirred mixture of iron oxide nanocrystal dispersion and CNTs (sieve fraction of the grains 200–400 μm) in octadecene was heated up from room temperature up to 200 °C (ramp of 15 °C min^{-1}) under inert atmosphere. The reaction mixture was sampled at different times, by fast withdrawing a small volume (about 200 μL) of the mixture at different time intervals during the heating process, and analyzing the sample by using transmission electron microscopy (TEM). The sample withdrawn after about 7 min heating, at a temperature of 130 °C, consisted of nanocrystals densely packed on the external surface of CNT aggregates, while most nanocrystals were still in solution (**Figure 2**a). Samples taken when the mixture was at the final temperature of 200 °C and kept at this temperature for 2 min, consisted of both unattached and attached nanocrystals (Figure 2b). After holding the temperature at 200 °C for 30 min, the sample taken displayed a uniform distribution of nanocrystals attached to the CNTs (Figure 2c). Similar results were obtained for 67 nm iron oxide and 10 nm iron nanocrystals, respectively (Figures S1 and S2 in the Supporting Information). These results could be understood from the temperature-dependent diffusion rate of the Fe nanocrystals through the CNT grains. These CNT supports have a low density, with a total pore volume of 1.2 mL g^{-1} between entangled nanotubes.[40,41] When Fe nanocrystals and CNT particles are mixed together at low temperature, Fe nanocrystals can easily anchor on the external surface of the CNT aggregate, which is inferred from TEM, but they have limited access to the inner core of the CNT grain. This may be responsible for the apparent high local loading of the nanocrystals on the support at early reaction stages. On the other hand, heating at 200 °C for a longer time promotes Fe nanocrystals diffusion through the CNT skein and their attachment thereon. This result suggests that the nanocrystals attach reversibly to the surface of the CNTs at 200 °C, so that those particles which initially attach to the external surface of the CNT grains can detach and diffuse to the inner core of the CNT grains at longer reaction times. At thermodynamic equilibrium, the nanocrystals were homogeneously dispersed on the CNT surface available, both at the surface and in the core of the CNT grains.

For comparison, we performed a similar experiment in which iron oxide nanocrystals were injected directly at high temperature in a suspension of finely dispersed CNTs, so that diffusion of nanocrystals through the very small grains does not play a major role in the Fe–CNT formation. Interestingly, the samples withdrawn at different time intervals, analyzed using TEM, had a comparable loading and distribution of iron nanoparticles, thus indicating that already 3 min after injection the iron oxide nanocrystals were attached to the CNTs and this Fe–CNT structure was stable over time (Figure S3 in the Supporting Information). This result indicates that nanocrystals can rapidly adsorb at the CNT surface and the attachment of nanocrystals to larger grains of entangled CNTs is dominated by a dynamic process of adsorption and desorption in combination with diffusion of nanocrystals.

By considering that the colloidal nanocrystals diffuse in the liquid phase (octadecene), we calculated the diffusion coefficient from the Einstein–Stokes formula:

$$D = kT/(6\pi\eta R), \tag{1}$$

where k is the Boltzmann constant, T is the temperature, η is the viscosity of the solvent, and R is the hydrodynamic radius of the colloidal nanocrystal. By considering that the CNTs have density of ≈2 g mL^{-1} and a total pore volume of ≈1.2 mL g^{-1},[40,41] it follows that the porosity amounts to 70%. Due to the large void fraction, it can be considered that the nanocrystal diffusion rate mainly depends on the octadecene viscosity, the nanocrystal hydrodynamic radius, and the temperature. We calculated the diffusion path length of a nanocrystal in pure octadecene by using the formula:

$$t = L^2/D, \tag{2}$$

where t is time, L is the diffusion path length of the nanoparticles, and D is the diffusion coefficient. After heating at 200 °C ($D = 1.7 \times 10^{-10}$ m^2 s^{-1}) for 30 min, the path covered by the particles will be in the order of a millimeter. It is then reasonable to say that the diffusion path of colloidal nanocrystals is comparable to that of the support grain size and a uniform distribution of nanocrystals over the CNT bodies can be realized.

A TEM study of sectioned samples was also performed to further verify the homogeneity of the Fe nanocrystal dispersion within the CNT grains (**Figure 3**). Due to the large void fraction, slices through CNT grains appeared at TEM as "islands" of packed CNTs in the size range of tens of micrometers, partially interconnected. An illustrative example of an 8 nm iron

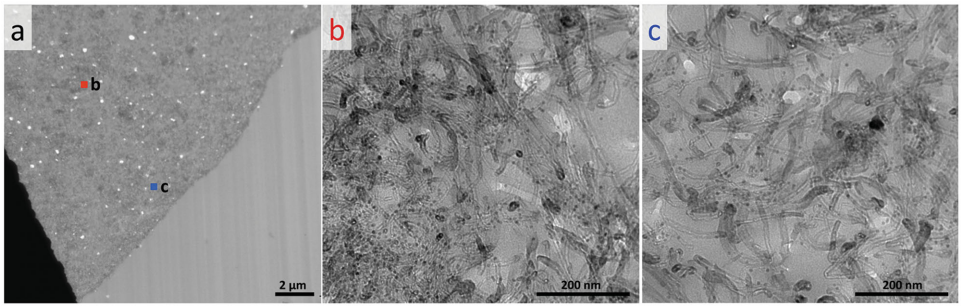

Figure 3. a) TEM image of a slice of an Fe–CNT catalyst embedded in polymer. Two different areas, indicated with a red and a blue square, are imaged at higher magnification in the TEM images in panels (b) and (c), respectively.

oxide nanocrystal catalyst is presented in Figure 3, showing TEM images of an Fe–CNT grain microtomed slice (about 50 μm large), where the two areas indicated in blue and red were imaged with higher magnification in the right figure panels (b) and (c). In Figure 3, it is shown that both in the center (Figure 3b) and in the perimeter (Figure 3c) of the hybrid Fe–CNT microparticle the iron nanocrystal distribution was homogeneous. A uniform nanocrystal distribution was observed by measuring several areas. Similarly, by analyzing microtomed sections (of 20–50 μm size) of a catalyst containing Fe nanocrystals of about 4 nm diameter, nanocrystals were uniformly distributed both in the perimeter and in the center of the microtomed slice of Fe–CNTs. This observation is a direct proof that the iron nanocrystals were not solely attached to the external CNT grain surface. For comparison we also analyzed an Fe–CNT sample containing iron oxide nanocrystals of 14 nm. By observing several microtomed slices at TEM, we occasionally found a slight difference in nanocrystal distribution between the external and the internal areas of the grain slice. In particular, within a few micrometers from the external edge of the catalyst slice there was a higher density of nanocrystals, while in the core (more than 10 μm from the external surface) there were few nanocrystals, or, in some analyzed areas, no nanocrystals at all, possibly because the size of the nanocrystals got closer to that of the maximum in the mesopore size distribution of the CNT grains (30–40 nm).[40]

In general, the procedure described here allowed us to fabricate Fe–CNT composites consisting of iron/iron oxide nanocrystals with tunable diameter in the 3–20 nm range uniformly anchored to the CNT supports (**Figure 4**a–d), with the additional advantage that the iron loading and nanocrystal size could be tuned independently. The metal loading, verified by thermal gravimetric analyses (TGAs), could be tuned in the 2–30 Fe wt% simply by changing the proportion of iron nanocrystals injected to CNTs (Figure S4 in the Supporting Information).

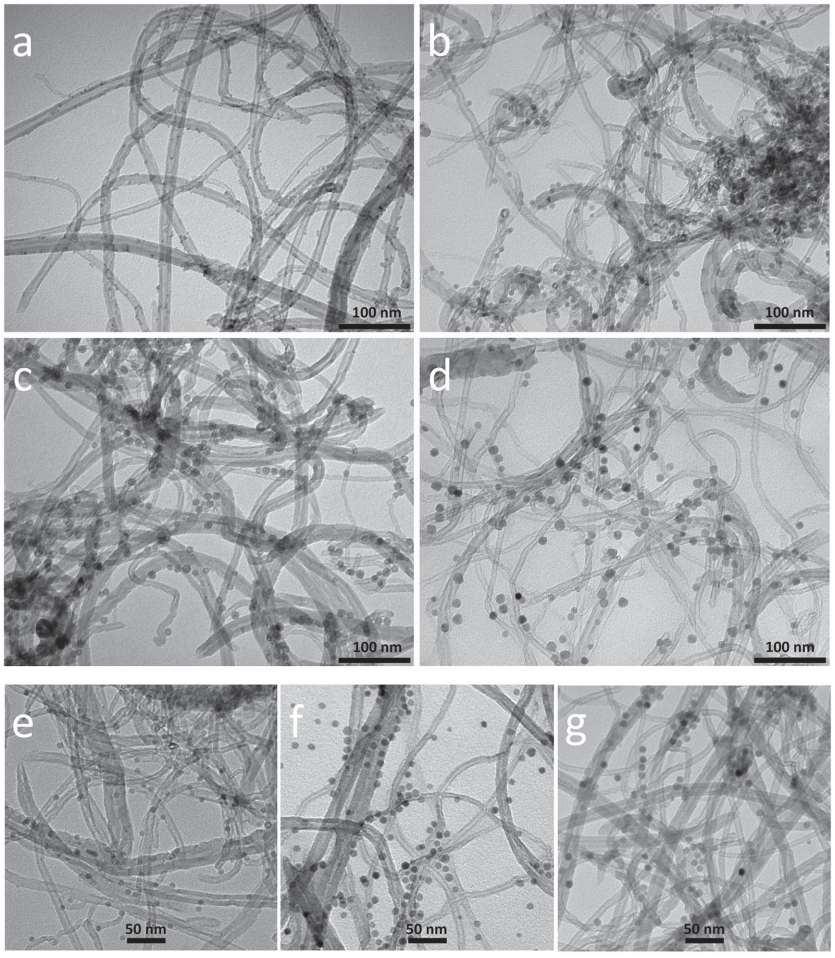

Figure 4. a–d) TEM images of Fe–CNT catalysts consisting of nanocrystals of different sizes: a) 3 nm nanocrystals 6 wt% iron loading; b) 8 nm nanocrystals 8 wt% iron loading; c) 10 nm nanocrystals 5 wt% iron loading; d) 14 nm nanocrystals 5 wt% iron loading; obtained when small amounts of ligands are present in the reaction mixture. e–g) TEM images of Fe–CNT catalysts obtained with different amounts of ligands in the reaction mixture: e) 8 nm nanocrystals on CNT obtained by addition of 100 μL oleylamine where most of the nanocrystals are attached to the CNTs; f) 10 nm nanocrystals on CNT obtained by addition of 500 μL oleylamine, showing that most of the nanocrystals are freestanding; g) 10 nm nanocrystals on CNT obtained in absence of additional ligands.

The attachment of iron oxide nanocrystals to CNTs was strongly affected by the amount of surfactants, typically a mixture of oleic acid, oleylamine, and 1,2-hexadecanediol, present in the mixture. When the nanocrystal suspension was purified repeatedly (three to six cycles) with toluene/isopropanol to remove the excess of ligands from the nanocrystal surface, the sample showed iron nanocrystals anchored to the CNT surface (Figure 4a–d, g). TEM of these samples prior to drying did not show more than 2% free (detached) nanocrystals (Figure 4g). On the other hand, by increasing the amount of ligands still present in solution, a higher amount of unbound, free nanocrystals was observed (Figure 4e,f, and Figure S5 in the Supporting Information). This appeared to be the case when (i) the nanocrystals were grown in situ in the presence of CNTs and excess of ligands; (ii) the nanocrystal suspension was not efficiently purified (one to two precipitation cycles only); (iii) small amounts of ligands (in the order of hundreds microliters) were purposely added to the mixture (Figure 4e,f). In particular, about 5%–10% free particles were observed when 100 µL oleylamine was added on purpose (Figure 4e), while there were more than 50% free particles when 500 µL oleylamine was injected (Figure 4f, and Figure S5 in the Supporting Information). These results demonstrate that by changing the amount and nature of the ligands it was possible to control the attachment of the Fe nanocrystals on the CNTs.

These results are consistent with previous studies by Ritz et al. showing that CNTs can act as ligands on the surface of colloidal nanocrystals and replace surfactants on the nanocrystal surface,[42] rather than by assembly via ligand adsorption on the graphitic surface.[43] Ritz et al. [42] showed that the graphitic surface of nonfunctionalized CNTs can attach to the surface of metallic colloidal nanocrystals by a partial electron-donor effect, thus coordinating the metal at the surface. From our experimental observation, higher amounts of ligands (approximately more than one monolayer) can shield the nanocrystal surface, making nanocrystal more stable in solution and limiting nanocrystal–nanocrystal as well as nanocrystal–CNT interactions. During the heating process, the nanocrystals were stabilized either by free ligands and/or by CNTs. Thus, the sample at any time would consist of a mixture of particles attached and detached to the CNT support. On the other hand, when the nanocrystals were repeatedly purified and freed from the excess of surfactants, they would increase their surface energy. Once the CNTs are adsorbed at the nanocrystal surface they could act as ligands and passivate the dangling bonds at the nanocrystal surface and decrease the nanocrystal surface energy. At high temperature, the attachment of the CNTs on the Fe nanocrystal surface is a reversible process, but the presence of a large excess of CNT could shift the equilibrium toward the formation of Fe nanocrystal–CNT composites. We propose that the Fe nanocrystals attach to the CNT surface via noncovalent bonds and the CNT structure is preserved, as also confirmed by high-resolution TEM (HRTEM) study (**Figure 5**).

A better insight in the nanocrystalline structure was obtained by HRTEM and scanning TEM (STEM) (Figure 5a–d), showing monocrystalline nanocrystals in a cubic phase attached to the external surface of the CNTs. The high-resolution image in Figure 5b displays a monocrystalline nanocrystal with lattice distances of 0.24 and 0.29 nm, measured from the fast Fourier

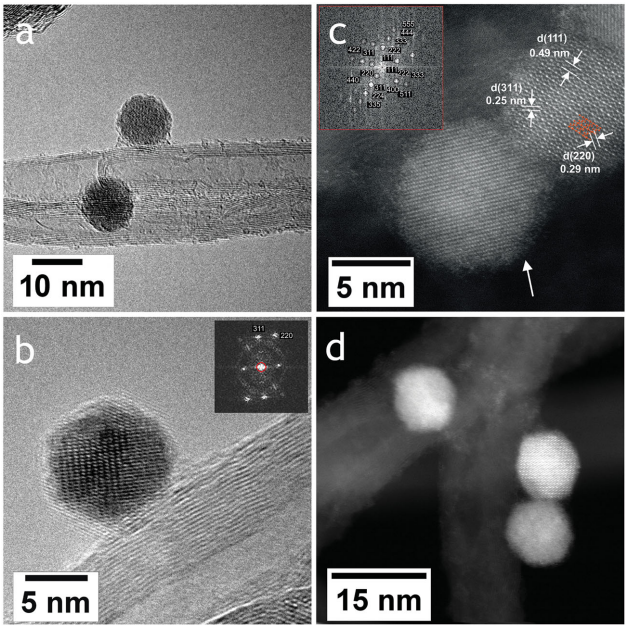

Figure 5. a,b) High-resolution TEM, and c,d) scanning TEM (STEM) images of iron oxide nanocrystals 10 nm diameter immobilized on CNTs. The insets show the fast Fourier transform (FFT) spectrum. c) STEM image showing monocrystalline nanocrystals in a cubic phase with measured lattice distances. The crystal structure is consistent with the theoretical crystal structure of Fe_2O_3 (oxygen is hidden) overlaid in red. The lower particle is most probably oriented along the [1,6,3] direction. The nanocrystallites are covered with the remaining ligand shown as an amorphous shell (see arrow).

transform (FFT) spectrum, corresponding to the [311] and [220] of Fe_2O_3. On the side of the nanocrystal, a low-contrast spot may be attributed to carbonaceous deposits (Figure 5a,b), which may be formed at the CNT–iron oxide interface by decomposition of the organic ligands under drying conditions. The STEM image in Figure 5c shows monocrystalline nanocrystals with measured lattice distances of 0.49, 0.25, and 0.29 nm, respectively, consistent with the theoretical structure of Fe_2O_3. The nanocrystallites were covered with an amorphous carbon shell of ligands (as indicated by the arrow in Figure 5c), since the latter Fe–CNT sample was isolated solely by precipitation and without a specific drying procedure. All images show that the interface between nanocrystal and CNT graphitic surface is distinct and sharp, pointing to the formation of a significant Fe–CNT interaction. We studied the reciprocal orientation between interfacial iron oxide crystallographic facets and the graphitic planes of CNT surface, but not specific preferential or epitaxial crystallographic orientation was found.

X-ray diffraction (XRD) measurements were performed to determine the crystallinity of the nanocrystals and the size of the crystallites from the diffraction line broadening, as shown in **Figure 6**a. Due to the small nanocrystal size, XRD showed broad peaks, which were attributed to the cubic spinel phase, confirming that the sample composition was homogeneous for the bulk of the catalyst. By comparing the peak for the (311) diffraction line, which is expected to be the most intense peak with no overlapping with CNT peaks, for different Fe–CNT samples, we were able to correlate the crystallite average size with the

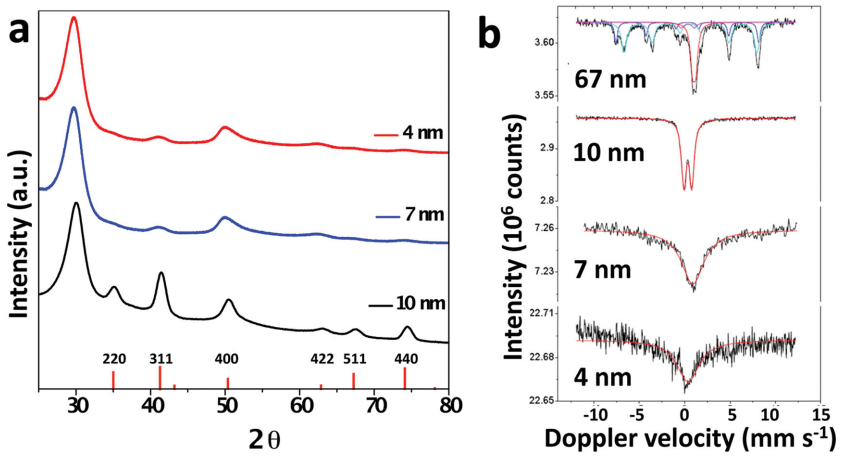

Figure 6. a) X-ray diffraction (XRD) pattern of catalysts consisting of iron oxide nanocrystals of 4, 7, and 10 nm diameter, respectively, attached to CNTs. The intensity has been normalized to the maximum, which is the peak at 29.8°, attributed to graphite. For comparison, the standard XRD pattern of iron oxide (γ-Fe_2O_3/Fe_3O_4) is reported in red. In the sample with 10 nm nanocrystals the higher intensity of the iron peaks compared to the C peak can be attributed to the higher iron loading of this sample, around 13 Fe wt%, as compared to the 4 Fe wt% of the other two samples. b) Mössbauer spectra of Fe–CNT catalysts with ≈5 wt% iron loading, with iron oxide nanocrystals of 4, 7, 10, and 67 nm, respectively.

Fe nominal nanoparticle size determined by the TEM-based statistics. By decreasing the nominal nanoparticle size from 10 to 4–7 nm, we observed a broadening of the (311) peaks, accordingly with the decrease in the crystallite average size. Mössbauer spectroscopy gave more insight into the structure, revealing that nanocrystals certainly contain Fe^{3+} species (possibly γ-Fe_2O_3, Figure 6b). Only nanocrystals of around 70 nm diameter (67 ± 8 nm), which were synthesized by a different procedure,[39] consisted of a mixture of magnetite and maghemite phases (Figure 6b, top spectrum).

The iron oxide nanocrystal-decorated CNTs were finally investigated as catalysts for FTO conversion. An important requirement for the application of colloidal nanocrystal-based nanocomposites as heterogeneous catalysts is the complete removal of surfactants on the Fe nanocrystals, since residual oleate/oleyalamine ligands would affect the accessibility to active sites. An efficient drying/activation method is therefore required. In the optimized drying procedure, the catalysts were washed repeatedly in hexane and acetone (for more details refer to the Experimental Section). For the solvent removal, they were first dried in static air, at 60 °C for 1 h and at 120 °C for 3 h (step 1), and successively under vacuum and heating at 80 °C for 3 h (step 2). This second step was crucial to eliminate the excess of solvent and ligands present. Thermal gravimetric analyses combined with mass spectrometry (TGA–MS) were performed on the same catalyst at different drying stages in order to study the mass loss (**Figure 7**a,c, black line) and the formation of oxidation products while applying a temperature ramp under oxygen flow (Figure 7a–c). By comparing the TGA plots of samples taken before and after drying in vacuum, we observed different trends. In the first sample, isolated before drying in vacuum, shown in Figure 7a,b, a small weight loss was observed between 200 and 400 °C, accompanied by several MS peaks, attributed to H_2O, CO_2, and CO with a maximum around 350 °C. The enlargement of the graphs in this temperature range in Figure 7b shows an additional peak of m/z 55 (carbon cation $C_4H_7^+$, base peak of hydrocarbon ions $C_{2n}H_{2n-1}^+$) a characteristic peak of oleic acid and oleylamine ligands, as well as of octadecene solvent. The weight loss in this sample (Figure 7a,c black line) occurring around 350 °C could be attributed to the decomposition of the residual coordinating solvents (ligands), at high temperature under oxidizing conditions, into water and carbon oxides. When an additional vacuum treatment was applied (drying step 2), the TGA–MS did not show carbon weight loss nor any relevant MS peak below 500 °C, indicating the effective removal of residual ligands (Figure 7c,d).

This drying procedure allowed the elimination of the excess of organic molecules, nevertheless residual ligands tightly bonded to the nanocrystal surface could still be present. In this regard, a high-temperature treatment of the catalyst allows elimination of the organic molecules, provided that the temperature is not too high to cause nanocrystal re-shaping and ripening.[44,45]

The iron oxide catalysts were reduced in situ under diluted H_2 flow (H_2:Ar of 1:2) at low pressure and successively tested for FTO synthesis at 350 °C, at 1 bar and low CO conversion to allow differential operation, at a CO to H_2 volume ratio of 1:1. This general procedure, optimized elsewhere,[6,8] was used to first reduce iron oxide into metallic iron, which under successive syngas exposure was converted into iron carbide, known to be the active phase for FTO synthesis. We compared the catalyst activity, expressed as iron time yield (FTY) over time on stream (**Figure 8**) for catalysts that underwent different reduction conditions, namely by reducing at 350 °C (T350), 450 °C (T450), and while ramping the temperature from 70 to 350 °C (T70–350), showing that reduction at constant temperature gave the highest activity over time. An increase in reduction temperature from 350 to 450 °C enhanced the activity, this effect being more evident during the first hours on stream, while it did not affect the product selectivity significantly (Figure 8, **Table 1**). A possible explanation is that higher activation temperatures favor the conversion of iron oxide into the active phase, through the formation of metallic iron, thus leading to higher overall activity of the catalyst. Nevertheless, the T450 catalyst deactivated fast in the first hours on stream, leading to activities similar to those of sample T350. The spent catalysts T350, T450, and T70–350 were analyzed at TEM to detect structural transformations (Figure S6 in the Supporting Information) after syngas exposure. Sample T350 showed unchanged nanocrystal size and distribution on the CNTs compared to the fresh catalyst (Figure S4a in the Supporting Information), pointing to the absence of sintering/ripening effects after long exposure to syngas and heating. The appearance of low contrast areas around the nanocrystals pointed to the formation of amorphous carbon deposits (Figure S6a in the Supporting Information). On the other

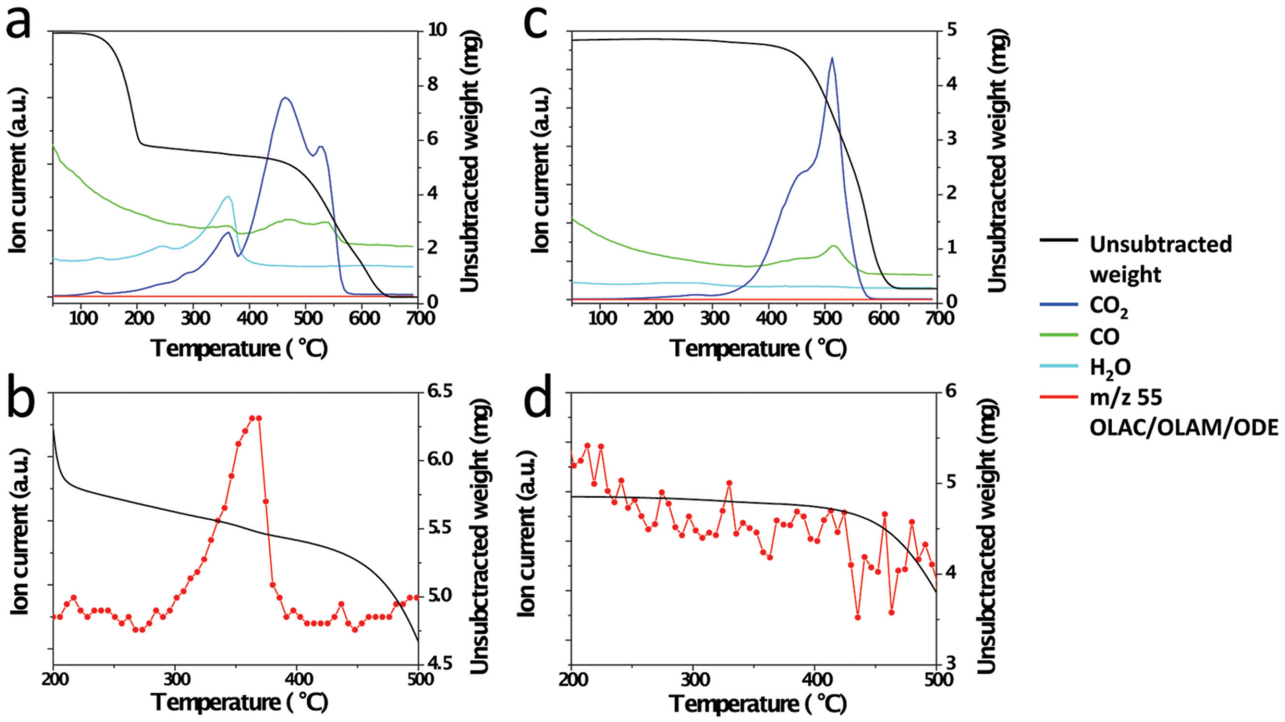

Figure 7. Thermal gravimetric analysis–mass spectrometry (TGA–MS) curves of Fe–CNT catalysts a,b) after drying in static air and c,d) after an additional drying step under vacuum. Unsubtracted weight measurements are reported in black. b–d) Enlargement of the thermogravimetric curves in the 350 °C region.

hand, in both T450 and T70–350 spent catalysts the nanocrystal size distribution appeared broadened, with a maximum at 7 nm (Figure S6b,c in the Supporting Information), higher than the average 4.3 nm size of the fresh catalyst (Figure S4a in the Supporting Information). Interparticle spacing was higher, pointing to the occurrence of nanocrystal growth. T450 and T70–350 activation conditions lead to more aggregation, possibly due to the different transformation paths the samples have been going through. Nevertheless, in all the studied catalysts the average nanocrystal growth under FTO conditions was to a limited extent only (less than 100%) compared to conventional catalysts (average particle size growth of more than 200%), pointing to a remarkable structural stability. It is clear from TEM of both spent catalysts that carbon deposits had formed on the nanocrystal surfaces for all samples. Being carbon one of the side products of FTO synthesis, the nucleation of carbon on the metal nanocrystals was accounted for the main catalyst deactivation path.

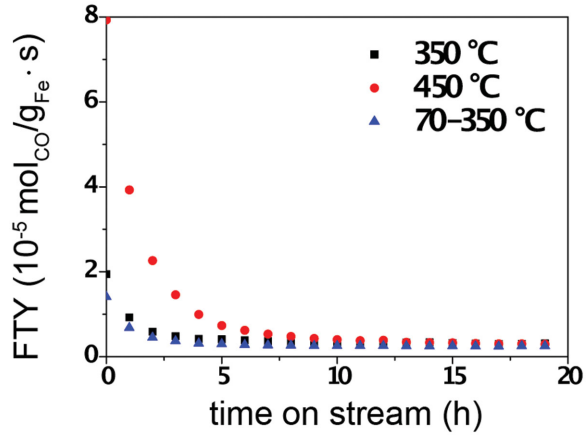

Figure 8. Effect of the reduction step temperature on the catalyst activation for a catalyst consisting of 4.3 nm iron nanocrystals attached to CNTs: plot of the iron time yield (FTY) over time on stream for catalysts reduced at 350, 450, and in the 70–350 °C range.

Table 1 shows the catalyst activity (FTY), and the product selectivity at 15 h on stream of syngas, when the system has reached stabilization. By comparing the catalytic performance of T350 catalysts based on colloidal particles of 4.3 ± 0.4 nm iron oxide nanocrystals with that of catalysts obtained by impregnation of carbon nanofibers (iFe–CNF) with 4 ± 0.9 nm iron oxide particles,[6] we observed that Fe–CNT samples showed comparable activity and selectivity when tested in similar conditions (Table 1). Activity versus time on stream of the T350 catalysts is also reported in **Figure 9**a, black line. Colloidal Fe–CNT catalysts compared to an iFe–CNF catalyst showed higher olefin selectivity (59% C vs 50% C) and advantageous lower methane selectivity (29% C vs 36% C). The catalysts followed the Anderson–Schulz–Flory product distribution (Figure 9c) with a chain growth probability (alpha) of 0.43, which falls in the range of the maximum C_2–C_4 selectivity achievable. For comparison, catalysts consisting of nanocrystals of 3, 7, 10, and 14 nm with narrow size distribution (Figure S7 in the Supporting Information) were tested in the same conditions, after reduction at 350 °C. For all sizes, the catalyst activity, measured as the iron time yield at different time on stream, decreased over time, possibly deactivating due to the formation of carbon

Table 1. Activity and product selectivity of Fe–CNT catalysts with about 5 Fe wt% under FTO conditions (1 bar, 350 °C, $H_2/CO = 1/1$) after 15 h on stream. The samples are: 4.3 nm iron oxide nanocrystal catalysts after reduction at different temperature conditions (T350, T450, T70–T350) compared to iFe–CNF catalyst (from ref. [6]); catalysts with iron oxide nanocrystal size of 3, 7, 10, and 14 nm after reduction at 350 °C.

Sample	Nanocrystal size [nm]	FTY 15 h on stream [10^{-5} mol_{CO} $(g_{Fe}$ $s)^{-1}$]	Product selectivity [% C] 15 h on stream			
			CH_4	C_2–C_4 olefins	C_{5+}	C_2–C_4 paraffins
Fe–CNT_T350	4.3	0.32	29	59	9	3
Fe–CNT_T450	4.3	0.33	31	57	10	2
Fe–CNT_T70–350	4.3	0.25	31.5	56	9	3.5
iFe–CNF	4	0.39	36	50	11	3
Fe–CNT_3 nm	3	0.38	32	54	11	3
Fe–CNT_7 nm	7	0.19	31	60	7	2
Fe–CNT_10 nm	10	0.12	38	52	7	3
Fe–CNT_14 nm	14	0.11	38	52.5	7.5	2

deposits (Figure 9a), while for all samples the product distribution over time did not change significantly (Figure 9b, and Figure S8 in the Supporting Information). By increasing the nanocrystal size, the catalyst activity decreased accordingly with the increase of catalytic surface area exposed (Figure 9a), which could be accounted as the dominating factor affecting size-dependent activity. However, other factors, such as size-dependent reducibility and carbidization, could also play a role. On the other hand, the product distribution did not change significantly with the catalyst nanocrystal size (Table 1), with alpha values in the range of 0.35–0.43 as inferred from the Anderson–Schulz–Flory plots (Figure 9c and Figure S9 in the Supporting Information). These results show that catalysts obtained by colloidal nanocrystals have comparable catalytic properties than those of catalysts obtained by conventional, ligand-free methods like incipient wetness impregnation, with the advantage that the catalysts properties can be more precisely controlled and tuned. These new catalysts could be used as model systems for the study of in situ catalyst transformation and shed light on fundamental structure-sensitive processes, like catalyst deactivation by coke laydown and promoter effects.

3. Conclusions

In conclusion, we have developed a new method to assemble iron-based catalysts consisting of monocrystalline iron and iron oxide nanocrystals with controlled sizes in the 3–20 nm range and a narrow size distribution. These nanocrystals were attached and appeared to be homogeneously distributed over the surface of nonfunctionalized CNT supports. Iron loading was tuned by adjusting the nanocrystals to CNT ratio. The formation of Fe–CNT hybrid structures was regulated by controlling the temperature and the amount of ligands, thus promoting the penetration of Fe nanocrystals within the skein of CNT grains and their reversible attachment to the graphitic surface of the CNTs. Under conditions optimized in our experiment, the nanocrystals were homogeneously distributed within the CNT support, producing a fine dispersion of the catalyst. A simple drying procedure allowed us to eliminate residual organic ligands. We finally demonstrated that these catalysts with controlled structural characteristics were active for the Fischer–Tropsch conversion of syngas, selective for lower olefin products and showed high resistance to particle growth.

4. Experimental Section

All chemicals were of the highest purity available and were used as received; iron pentacarbonyl ($Fe(CO)_5$, 99.99%), oleic acid 90%, oleyl amine 70%, 1,2-hexadecandiol ≥ 98%, 1-octadecene 90%, and diphenyl ether 99% were purchased from Aldrich. All solvents used were of analytical grade and were also purchased from Aldrich. Multiwalled carbon nanotubes (from 5 to 30 nm external diameter) with maximum 1% inorganic impurities were purchased from Bayer (Baytubes C 150 HP).

Iron Oxide Nanocrystal Synthesis: Iron oxide nanocrystals in the 3–14 nm range were synthesized according to the procedure published by Buonsanti et al.[36,37] A three-neck flask was loaded with 1.5 mmol of oleic acid, 0.75 mmol of oleylamine, and 1.25 mmol of 1,2-hexadecanediol in 10 mL of octadecene and connected to a Schlenk line through a reflux cooler. The mixture was degassed for 20 min at 120 °C under low pressure and then purged under nitrogen flow. 1 mmol of $Fe(CO)_5$ was then injected and the mixture was heated by a ramp of 15 °C min^{-1} to reflux for 1 h under continuous stirring. Finally, the mixture was cooled down to room temperature and processed in air. The nanocrystal suspension was purified by four cycles of precipitation in isopropanol redispersion in a few drops of toluene. In the last step, the particles were finally dissolved in 8 mL octadecene. This general procedure produced particles of 5–7 nm. Smaller particles of 3–4 nm were synthesized by controlling the heating ramp at 5 °C min^{-1} around the nucleation stage (which typically takes place between 260 and 275 °C) up to 280 °C. Further growth of the nanocrystals up to 10–14 nm was accomplished by performing multiple injections of precursor at time intervals of 1 h. In this procedure 1 h after the first injection, a mixture of 1 mmol $Fe(CO)_5$ and 0.2 mL oleic acid in 1 mL octadecene was injected drop wise at a rate of 0.1 mL min^{-1} and the mixture was kept at this temperature for 1 h.[36,37]

For comparison, nanocrystals of about 70 nm diameter were synthesized according to the method published by Colvin and co-workers.[39] 2 mmol of Fe (III) acetylacetonate, 9 mmol oleic acid, and 5 g octadecene were loaded in a three-neck flask and degassed at 120 °C for 30 min, then heated in nitrogen under stirring to 320 °C and kept at this temperature for 30 min. After cooling down to room temperature the nanocrystals were finally purified by three cycles of precipitation in isopropanol and redispersed in toluene.

Iron Nanocrystal Synthesis: 10–20 nm iron nanocrystals were synthesized according to the method published by Cabot et al.[38]

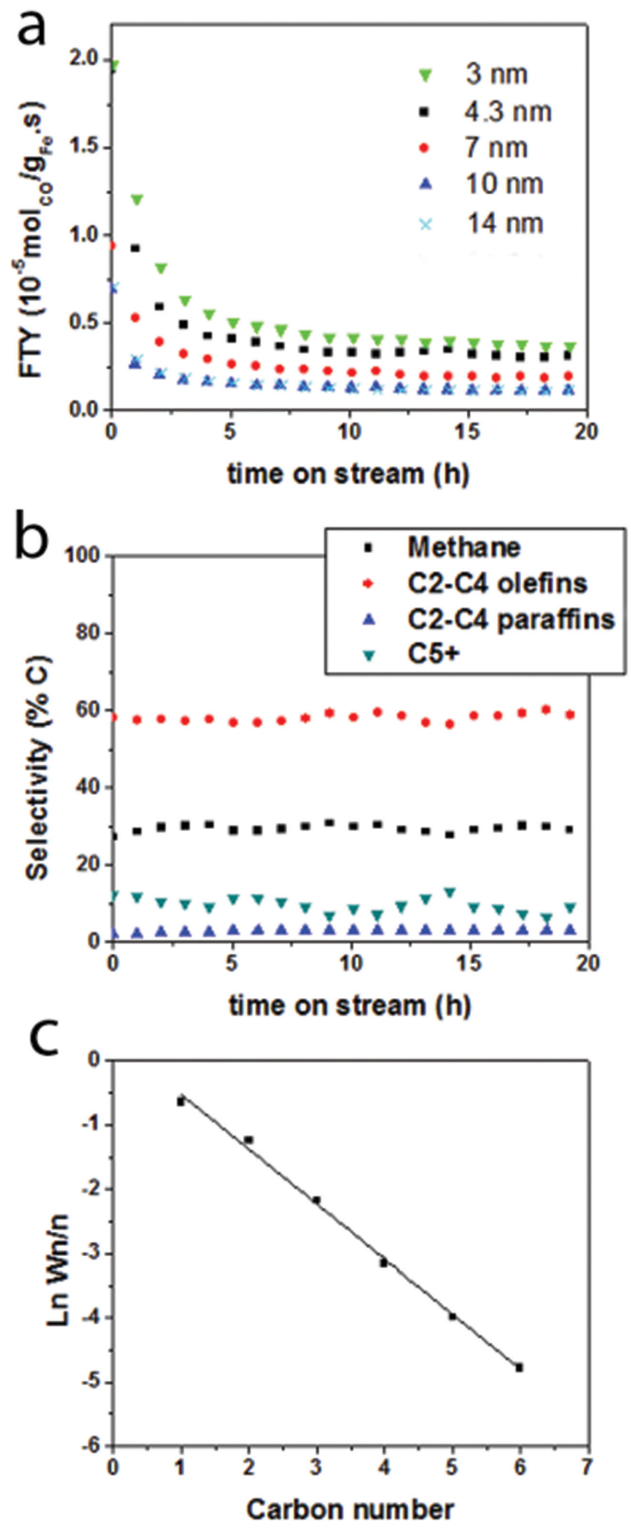

Figure 9. a) Iron time yield (FTY) over time on stream for catalysts consisting of iron oxide nanocrystals of different sizes in the 3–14 nm range. b) Product selectivity over time on stream and c) Anderson–Schulz–Flory plot for a catalyst consisting of 4.3 nm iron oxide nanocrystals on CNTs. The chain growth probability (alpha) is 0.43, Wn being the weight fraction of product with *n* carbon atoms at 19 h on stream. The data are measured at 350 °C, 1 bar H_2/CO ratio of 1.

A three-neck flask was filled with 0.67 mmol oleylamine and 10 mL ODE, degassed under vacuum at 120 °C for 1 h. The mixture was then heated up to 220 °C and 3 mmol of $Fe(CO)_5$ in 2 mL degassed octadecene were fast injected. After injection, the temperature was allowed to recover and kept at 220 °C for 15 min. The suspension was cooled down to room temperature. When the mixture reached about 100 °C, 0.3 mL of previously degassed oleic acid were injected in order to improve the nanoparticle dispersion and avoid aggregation and sintering. The nanocrystals were then recovered by addition of toluene, and successively purified by three cycles of precipitation in isopropanol and centrifugation, redispersion in toluene. In the last step, the particles were finally dissolved in 10 mL octadecene.

Fe–CNT Hybrid Structure Synthesis: In a typical synthesis of Fe–CNT hybrid structures with ≈5 wt% Fe loading, 750 mg of multiwalled CNT grains (sieved fraction 0.2–0.4 mm), 10 mL octadecene, and 5.5 mL of a concentrated suspension of iron oxide nanocrystals in octadecene (10 mg mL^{-1}) were loaded in a round flask, degassed at 120 °C for 15 min, successively heated up to 200 °C under nitrogen flow and stirring (400 rpm). The reaction mixture was kept at this temperature for 30 min, it was then allowed to cool down to room temperature and 5 mL hexane were added. At this stage, it was possible to have an indication of the success of the Fe nanocrystal attachment, since there was a direct correlation between the color of the suspension and the percentage of nanocrystals attached to the CNTs (Figure S5 in the Supporting Information). When the surnatant appeared clear and colorless, TEM showed that the surnatant contained no particles, while the precipitate consisted of nanoparticles directly connected to the surface of the CNTs (Figure S5, right panel, Supporting Information). On the other hand, an inefficient formation of hybrid Fe–CNT particles (when, for example, ligands were purposely added to the suspension) could be detected by the formation of a brownish surnatant, since unattached iron nanocrystals were soluble in hexane, conferring the surnatant a dark-brown color. When investigated at TEM, both the brownish surnatant and the dark-black precipitate showed free nanocrystals, not attached to the CNT support (Figure S5, left panel, Supporting Information).

Purification/Drying of Fe–CNT Hybrids: The suspension was finally washed six times with hexane and acetone 1:3 and dried by heating in static air at 120 °C for 3 h and successively under vacuum for 3 h under slight heating at 80 °C.

Control Experiment Where CNTs were Dispersed in Solution: For this experiment, 5 mg CNTs were dispersed in 8 mL diphenyl ether and sonicated for 1 h. The mixture was then degassed under vacuum at 120 °C for 20 min and heated up to 200 °C under nitrogen atmosphere. 0.2 mg of iron oxide nanocrystals, previously dispersed in 2 mL diphenyl ether in a nitrogen-filled glove box, were then injected in the hot CNT dispersion at 200 °C and stirred at this temperature for a total of 2 h. The reaction mixture was sampled at 2, 10, 60, and 120 min, respectively, from injection by withdrawing small portions of the suspension and collecting them in a vial containing a few drops of hexane. The sample was then drop-casted on a TEM grid.

Catalyst Characterization (HRTEM, XRD, Ultramicrotomy, Mössbauer Spectroscopy, Thermogravimetric Analyses–Mass Spectrometry). TEM images were acquired on a Philips Tecnai-20 FEG (200 kV) microscope equipped with an EDX and HAADF detector. STEM images reported in Figure 5c,d were recorded at a spherical-aberration corrected 200 kV TEM/STEM with a cold field emission source and STEM probe corrector for spherical aberration (JEM-ARM200CF, JEOL, Japan). The probe current was of 0.25 nA, and the condenser lens aperture was 40 μm diameter. All recorded images had a size of 1024 × 1024 pixels. The contrast and brightness of each image shown were optimized for maximal visibility of the nanocrystals.

For the TEM sample preparation, in the time-dependent experiments the reaction mixture was diluted with a few drops of hexane and directly drop-casted on a pioloform/carbon-coated copper grid. For the final catalyst TEM characterization, the dried sample was mashed into a finer powder, a few drops of hexane were added, and sonicated for a few seconds to disperse the catalyst in the solvent. The suspension was finally drop-casted on the TEM grid.

XRD measurements were performed with a Bruker AXS D8 Advance diffractometer equipped with a $Co_K\alpha_1$ source (λ = 0.178897 nm) from 25° to 80° in 2θ.

TGAs were performed in a Perkin Elmer Pyris 1TGA instrument. The iron loading was determined by measuring the weight loss after heating the fresh catalyst from 30 to 700 °C (ramp 5 °C min^{-1}) under a 10 mL min^{-1} oxygen flow and after keeping the final temperature of 700 °C for 1 h.

The composition of the Fe phase before reaction was determined in situ with transmission ^{57}Fe Mössbauer spectroscopy. The spectra were collected at room temperature with a conventional constant acceleration spectrometer using a ^{57}Co (Rh) source. Velocity calibration was carried out using an α-Fe foil. The Mössbauer parameters were estimated by fitting the spectra using the Mosswin 4.0i program.

Drying Procedure: To assure a complete elimination of the ligands the catalysts were activated in diluted hydrogen at high temperature (350 °C to 450 °C) for 2 h. This step, prior to flowing synthesis gas in FTO conditions, also assured the reduction of iron oxide into metallic iron, which could more easily carburize and convert into active iron Hägg carbide (Fe_5C_2) under syngas flow. We investigated the effect of reduction temperature on the activation of Fe nanocrystal-decorated CNT catalysts. In order to study the effect of reduction temperature on the catalyst activity, catalysts consisting of 4.3 (±0.4) nm nanocrystals anchored on CNTs with an iron loading of 5 wt% were reduced in situ, prior to syngas flow, in a plug-flow reactor by flowing 33% hydrogen in argon at different temperatures, namely T350, T450, and T70–350. For experiments T350 and T450, the catalyst was heated under argon flow by 5 °C min^{-1} up to the final temperature of 350 and 450 °C, respectively. Once the final temperature was reached, hydrogen flow was introduced and the catalyst reduction was conducted at constant temperature for 2 h, before syngas was flown. For experiment T70–350, hydrogen flow was started at low temperature (70 °C) while the catalyst was heated by 5 °C min^{-1} up to 350 °C and was finally kept at this temperature, under hydrogen flow, for 2 h. After each reduction step, the temperature was stabilized to 350 °C and synthesis gas was fed for FTO in the conditions described below.

Activation and Fischer–Tropsch to Olefins Tests. The Fischer–Tropsch synthesis was performed at 1 bar and 350 °C using a mixture of H_2 and CO (1/1 v/v). H_2 (99,999%), CO (99%), and Ar (99,999%) were supplied by Linde Gas and used without further purification. An amount of 20 mg of the catalyst (particle size 0.2–0.4 mm, ρ = 0.2 g mL^{-1}) was diluted with 200 mg of SiC (particle size 0.2 mm) and placed in a plug flow reactor. The reaction was carried out at low CO conversions (<1%) to ensure differential operation. The catalysts were reduced in situ, prior to reaction, using a mixture of H_2 and Ar (33% v/v H_2; 60 mL min^{-1}) for 2 h (ramp 5 °C min^{-1}). In experiments T350 and T450, the catalysts were heated under Ar flow until the reaction temperature (ramp 5 °C min^{-1}) to the final temperature of 350 and 450 °C, respectively. Subsequently, the flow was switched to the H_2/CO mixture (6 mL min^{-1}). In the experiment T70–T350, the H_2/CO flow (6 mL min^{-1}) was switched during heating when the catalyst temperature was 70 °C and then heated up to 350 °C. The product selectivity to hydrocarbons up to C16 was determined with gas chromatography (GC) using a Varian CP3800 analyzer equipped with an FID detector (Column CP Sil 5 CB). The GC was calibrated with a gas mixture of known composition. The calibration for low concentrations was performed by dilution of the calibration mixture to ensure the reliability of the data at low CO conversions. CO_2 selectivity was not measured. The product selectivity was calculated on a carbon atom basis: (moles of product Y) × (carbon atoms in product Y)/(total carbon atoms in hydrocarbons produced). The catalytic activities expressed as moles of CO converted to hydrocarbons per gram of iron per second (FTY) were determined after 1 and 19 h of reaction.

Supporting Information

Supporting Information is available from the Wiley Online Library or from the author.

Acknowledgements

This research received funding from the Netherlands Organization of Scientific Research (NWO) in the framework of the TASC Technology Area "Syngas, a Switch to Flexible New Feedstock for the Chemical Industry (TA-Syngas)". The authors thank J. D. Meeldijk for catalyst microtomy and HRTEM; M. Ruitenbeek, A. C. J. Koeken, and M. Watson for helpful discussion; Dow Benelux and Johnson Matthey; E. Arzt for his support through INM.

Received: May 6, 2015
Revised: June 26, 2015
Published online: July 29, 2015

[1] F. C. Meunier, *ACS Nano* **2008**, *2*, 2441.
[2] A. T. Bell, *Science* **2003**, *299*, 1688.
[3] G. A. Somorjai, F. Tao, J. Y. Park, *Top. Catal.* **2008**, *47*, 1.
[4] M. Boudart, A. McDonald, *J. Phys. Chem.* **1984**, *88*, 2185.
[5] R. A. van Santen, *Acc. Chem. Res.* **2009**, *42*, 57.
[6] H. M. Torres Galvis, J. H. Bitter, T. Davidian, M. Ruitenbeek, A. I. Dugulan, K. P. de Jong, *J. Am. Chem. Soc.* **2012**, *134*, 16207.
[7] D. A. J. M. Ligthart, R. A. van Santen, E. J. M. Hensen, *Angew. Chem., Int. Ed.* **2011**, *50*, 5306.
[8] H. M. Torres Galvis, J. H. Bitter, C. B. Khare, M. Ruitenbeek, A. I. Dugulan, K. P. de Jong, *Science* **2012**, *335*, 835.
[9] H. M. Torrs Galvis, K. P. de Jong, *ACS Catal.* **2013**, *3*, 2130.
[10] M. D. Shroff, D. S. Kalakkad, K. E. Coulter, S. D. Ko hler, M. S. Harrington, N. B. Jackson, A. G. Sault, A. K. Datye, *J. Catal.* **1995**, *156*, 185.
[11] J. Cheng, P. Hu, P. Ellis, S. French, G. Kelly, C. M. Lok, *J. Phys. Chem.* **2010**, *114*, 1085.
[12] M. Luo, H. Hamdeh, B. H. Davis, *Catal. Today* **2009**, *140*, 127.
[13] G. Prieto, A. Martinez, P. Concepcion, R. Moreno-Tost, *J. Catal.* **2009**, *266*, 129.
[14] K. M. Bratlie, H. Lee, K. Komvopoulos, P. Yang, G. A. Somorjai, *Platinum Nano Lett.* **2007**, *7*, 3097.
[15] V. Iablokov, S. K. Beaumont, S. Alayoglu, V. V. Pushkarev, C. Specht, J. Gao, A. P. Alivisatos, N. Kruse, G. A Somorjai, *Nano Lett.* **2012**, *12*, 3091.
[16] P. T. Witte, P. H. Berben, S. Boland, E. H. Boymans, D. Vogt, J. W. Geus, J. G. Donkervoort, *Top. Catal.* **2012**, *55*, 505.
[17] A. Martínez, G. Prieto, *Catal. Commun.* **2007**, *8*, 1479.
[18] M. Trépanier, A. K. Dalai, N. Abatzoglou, *Appl. Catal., A* **2010**, *374*, 79.
[19] N. Hondow, R. O. Fuller, *J. Colloid Interface Sci.* **2014**, *417*, 396.
[20] S. Eriksson, U. Nylén, S. Rojas, M. Boutonnet, *Appl. Catal., A* **2004**, *265*, 207.
[21] N. Fischer, E. van Steen, M. Claeys, *Cat. Today* **2011**, *171*, 174.
[22] N. Fischer, B. Clapham, T. Feltes, E. van Steen, M. Claeys, *Angew. Chem.* **2014**, *53*, 1342.
[23] C. Yang, H. Zhao, Y. Hou, D. Ma, *J. Am. Chem. Soc.* **2012**, *134*, 15814.
[24] G. Melaet, W. T. Ralston, C.-S. Li, S. Alayoglu, K. An, N. Musselwhite, B. Kalkan, G. A. Somorjai, *J. Am. Chem. Soc.* **2014**, *136*, 2260.
[25] Y. Zhu, L. P. Stubbs, F. Ho, R. Liu, C. P. Ship, J. A. Maguire, N. S. Hosmane, *Chem. Catal. Chem.* **2010**, *2*, 365.
[26] N. S. Hondow, G. A. Koutsantonis, R. O. Fuller, H. Fansuri, M. Saunders, R. L. Stamps, D. Zhang, *New J. Chem.* **2010**, *34*, 1286.
[27] A. F. Gross, M. R. Diehl, K. C. Beverly, E. K. Richman, S. H. Tolbert, *J. Phys. Chem. B* **2003**, *107*, 5475.
[28] F. Rodriguez-Reinoso, *Carbon* **1998**, *36*,159.
[29] K. P. de Jong, J. W. Geus, *Catal. Rev.* **2000**, *42*, 481.
[30] P. Serp, M. Corrias, P. Kalck, *Appl. Catal., A* **2003**, *253*, 337.

[31] H. Xiong, M. A. M. Motchelaho, M. Moyo, L. L. Jewell, N. J. Coville, *J. Catal.* **2011**, *278*, 26.
[32] M. C. Bahome, L. L. Jewell, D. Hildebrandt, D. Glasser, N. J. Coville, *Appl. Catal., A* **2005**, *287*, 60.
[33] W. Chen, Z. Fan, X. Pan, X. Bao, *J. Am. Chem. Soc.* **2008**, *130*, 9414.
[34] R. M. Malek Abbaslou, A. Tavassoli, J. Soltan, A. K. Dalai, *Appl. Catal., A* **2009**, *367*, 47.
[35] E. van Steen, F. F. Prinsloo, *Catal. Today* **2002**, *71*, 327.
[36] R. Buonsanti, V. Grillo, E. Carlino, C. Giannini, M. L. Curri, C. Innocenti, C. Sangregorio, K. Achterhold, F. G. Parak, A. Agostiano, P. D. Cozzoli, *J. Am. Chem. Soc.* **2006**, *128*, 16953.
[37] R. Di Corato, P. Piacenza, M. Musarò, R. Buonsanti, P. D. Cozzoli, M. Zambianchi, G. Barbarella, R. Cingolani, L. Manna, T. Pellegrino, *Macromol. Biosci.* **2009**, *9*, 952.
[38] A. Cabot, V. F. Puntes, E. Shevchenko, Y. Yin, L. Balcells, M. A. Marcus, S. M. Hughes, A. P. Alivisatos, *J. Am. Chem. Soc.* **2007**, *129*, 10358.
[39] W. W. Yu, J. C. Falkner, C. T. Yavuz, V.L. Colvin, *Chem. Commun.* **2004**, 2306.
[40] J.-P. Tessonnier, D. Rosenthal, T. W. Hansen, C. Hess, M. E. Schuster, R. Blume, F. Girgsdies, N. Pfänder, O. Timpe, D. S. Su, R. Schlögl, *Carbon* **2009**, *47*, 1779.
[41] Thomas O. Eschemann, Wouter S. Lamme, Rene L. Manchester, Tanja E. Parmentier, Andrea Cognigni, Magnus Rønning, Krijn P. de Jong, *J. Catal.*, **2015**, *328*, 130.
[42] B. Ritz, H. Heller, A. Myalitsin, A. Kornowski, F. J. Martin-Martinez, S. Melchor, J. A. Dobado, B. H. Juarez, H. Weller, *ACS Nano* **2010**, *4*, 2438s.
[43] X. Li, Y. Quin, S. T. Picraux, Z. Guo, *J. Mat. Chem.* **2011**, *21*, 7527.
[44] Z. L. Wang, J. M. Petroski, T. C. Green, M. A. El-Sayed, *J. Phys. Chem. B* **1998**, *102*, 6145.
[45] R. Yu, H. Song, X.-F. Zhang, P. Yang, *J. Phys. Chem. B* **2005**, *109*, 6940.